Switching valley filtered current directions in multiterminal graphene systems

V. Torres [1], D. Faria [2], and A. Latgé [1]

[1] *Instituto de Física, Universidade Federal Fluminense, Niterói, Avenida Litorânea sn, 24210-340, Rio de Janeiro, Brazil*

[2] *Instituto Politécnico, Universidade do Estado do Rio de Janeiro, Nova Friburgo, 28625-570, Rio de Janeiro, Brazil*

(Received 5 January 2021; revised 8 March 2021; accepted 9 March 2021; published 24 March 2021)

Valley filtering processes have been explored in different graphene-based configurations and scenarios to control transport responses. Here we propose graphene multiterminal setups properly designed to obtain valley filtered currents in a broad range of energy, in addition to the possibility of controlling their directions. We explore graphene systems with extended mechanical foldlike deformations as an opportunity to enhance valley filtered transmission. The mixing between the electronic confinement effects due to a magnetic field and strain results in a selective drive of the current components in the quantum Hall regime. We adopt the mode-matching method within the Green's function formalism, allowing direct analysis of the strain effect on each valley transmission. We estimate a threshold map of confinement parameters, characterized by the magnetic, deformation, and setup lengths, to optimize valley filter transport processes and the proper switch of the valley polarized current directions.

DOI: 10.1103/PhysRevB.103.115437

I. INTRODUCTION

One of the challenges for optimal use of graphene is driven by the valleytronics in the search to take advantage of the extra degree of freedom given by its typical valleys, K and K' [1–8]. An appropriate design of the system is fundamental for controlling valley polarized currents, focusing on quantum computation applications [9]. Although advances have been reported, with proposals of systems that present valley splitting, measurements and applications are still limited. One significant achievement in this context was the development of a four-kink valley polarized router device based on graphene bilayers [10]. Moreover, several deformed graphene systems have been explored as strategic setups to modulate electronic responses [11–20]. In particular, valley-splitting occurrence and valley inversion were proven possible experimentally in a graphene quantum dot induced by the tip of a scanning tunneling microscope (STM) in strained graphene regions [21,22]. The splitting of valley polarized Landau levels (LLs) caused by the coexistence of pseudomagnetic and external magnetic fields was observed in strained graphene in the quantum Hall regime [22–24]. These measurements motivate further research on graphene strained systems with specific designs enabling the collection of valley filtered currents.

Valley filtered transport has been explored in different scenarios. Valley polarized currents were proposed based on a ballistic point contact with zigzag edges allowing polarity inversion by local application of a gate voltage [4]. Also, strain in graphene is known to raise the possibility of valley spatial separation. Depending on the deformation profile, it is possible to generate the valley polarized local density of states (LDOS) [3,12] in regions that work as waveguides for polarized currents [11,25,26]. Other works have explored valley filtered currents in graphene considering the valley spatial separation combined with different mechanisms, such as edge disorder, strain superlattices, external magnetic fields, and multiterminal configurations [11,13,16,27]. For example, graphene superlattices designed by out-of-plane Gaussian deformations are shown to improve the valley filter capabilities of a single perturbation, with the conductance exhibiting a sequence of valley filtered plateaus [16].

External magnetic fields are used as an alternative mechanism to enhance the valley spatial separation and valley filtering effects due to strain [22,23,26]. The external field introduces the time-reversal symmetry breaking, allowing the manipulation of valley currents in different directions. Additionally, since in the quantum Hall regime the energy levels are known for pristine systems, the effect of deformations becomes more evident [3,13,28–33]. The detection of valley polarized LLs was predicted recently in the LDOS calculation of foldlike deformed graphene [26]. The spatial evolution of the valley-dependent features is revealed by a braided structure correlated with the pseudomagnetic field fringes arising on strained graphene that may be observable in STM measurements. In the two-lead device, extra conducting channels were predicted due to the deformation, expected to be valley polarized. However, further analysis should be done to collect the polarized states in multiterminal geometries.

Here we explore different possibilities of filtering valley currents by conveniently attaching electronic contacts where the current may go through. The idea is to provide appropriate conditions to separate and detect valley polarized transport. We consider a four-terminal strained fold graphene system, with leads positioned transversely and longitudinally to the central conductor. Some states are confined in the deformation region, while other polarized states are pushed to the transverse leads, with valley filtered currents expected in a broader energy range depending on the strain intensity. We show that

by bringing the system into the quantum Hall regime, it is possible to switch the polarized current directions with filtered transport in the longitudinal terminals. We discuss the relevance of the system's different confinement parameters to obtaining valley filter transport and switching the valley polarized current directions.

Disordered effects are not considered in the theoretical description. Although edge-disordered effects could eliminate edge channels in a two-terminal zigzag nanoribbon device, valley polarization is preserved in the ribbon's central part with quasiballistic properties [11]. In the four-terminal system discussed here, as the transmission can be affected by the edge disorder, a real magnetic field is proposed to reduce such a disorder effect, guaranteeing the valley polarization in the central part of the system. Of course, if the disorder is randomly distributed in the entire system, a detailed investigation is required since destructive interferences due to overlapping states may make the valley filtered proposal difficult.

II. MODEL

We consider a system formed by a graphene central conductor with zigzag edges along the x direction, connected to terminals that are described by perfect semi-infinite nanoribbons, labeled L (left), R (right), T (top), and B (bottom). The contact widths with zigzag and armchair edges are L_Z and L_A, respectively, as shown in Fig. 1. The system is modeled by the first-neighbor tight-binding Hamiltonian, given by

$$H = \sum_{\langle i,j\rangle} \lambda_{ij} c_i^\dagger c_j + \sum_{l=1}^{4} \left(\sum_{\langle i,j\rangle} \lambda_{ij}^l c_i^{\dagger l} c_j^l + \sum_{\langle i,j\rangle} h_{i,j}^l c_i^{\dagger l} c_j^l \right), \quad (1)$$

where the first term describes the conductor's central region and the second refers to the four terminals, which are coupled to the central part by the hopping energy $h_{i,j}^l$. The modification in the hopping parameter due to mechanical deformations and an external magnetic field, applied perpendicularly to the system, is [34]

$$\lambda_{ij} = \lambda_0 e^{-\beta\left(\frac{l_{ij}}{a_c}-1\right)} e^{i\frac{2\pi e}{h}\Phi_{ij}}, \quad (2)$$

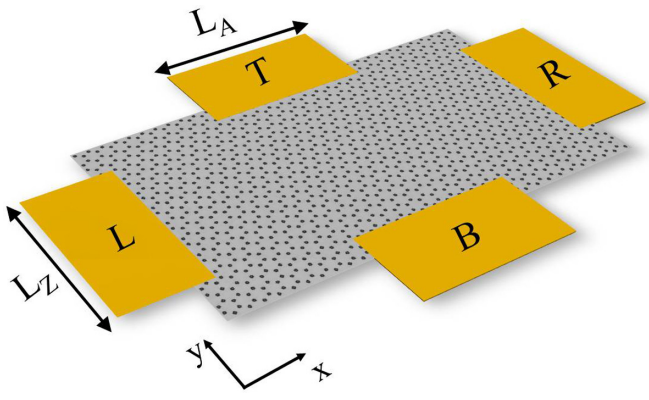

FIG. 1. Schematic representation of a graphene central conductor with zigzag edges along the x direction, contacted with semi-infinite graphene nanoribbons. Longitudinal leads, labeled L and R, have zigzag edges and width L_Z, while transverse leads, T and B, have armchair edges and width L_A.

where $\lambda_0 = 2.75$ eV, $\beta \approx 3$, $a_c = 1.42$ Å is the carbon-carbon distance in the unstrained system, and $l_{ij} = \frac{1}{a}(a^2 + \varepsilon_{xx}x_{ij}^2 + \varepsilon_{yy}y_{ij}^2 + 2\varepsilon_{xy}x_{ij}y_{ij})$ is the new distance between carbon atomic sites i and j, written in terms of the strain tensor $\varepsilon_{\mu\nu} = 1/2(\partial_\mu u_\nu + \partial_\nu u_\mu + \partial_\mu h \partial_\nu h)$ as a function of in-plane, $u_{\mu(\nu)}$, and out-of-plane, h, deformations, where μ and ν are the x and y directions. The deformation considered extends from the left to right contacts, along the zigzag direction, while the top and bottom leads are considered pristine armchair nanoribbons. The effect of a magnetic field $\boldsymbol{B}$ is introduced in the tight-binding Hamiltonian via the Peierls approximation [28], where the phase factor Φ_{ij} depends on the potential vector $\boldsymbol{A}$. The gauge was conveniently chosen to preserve the periodicity in the four terminals [35].

To explore the valley currents, we consider a foldlike deformation, representative of extended deformations usually found in graphene samples [22,23,36–42], defined as [11,26,43]

$$h = A_f e^{-\frac{(y-y_0)^2}{b^2}}, \quad (3)$$

where A_f and b denote the fold amplitude and extension, respectively, and $y_0 = L_Z/2$ corresponds to the deformation center. The parameter considered to indicate the deformation intensity is $\alpha = A_f^2/b^2$, which corresponds to a maximum strain intensity $\varepsilon_M = \alpha/e$, where e is Euler's number. Modifications in the hopping parameter due to the mechanical deformation give rise to a pseudogauge field in the continuum description [44–46], written as

$$\boldsymbol{A}_{ps} = \frac{\beta\hbar v_f}{2a_c}(\varepsilon_{xx} - \varepsilon_{yy}, -2\varepsilon_{xy}), \quad (4)$$

with v_f being the Fermi velocity. The pseudomagnetic field $\boldsymbol{B}_{ps} = \nabla \times \boldsymbol{A}_{ps}$ for this deformation exhibits a characteristic strip pattern that alternates between positive and negative field regions. It has opposite signs for electrons around each valley, allowing the production of valley current polarization on the pseudofield stripes [11].

A continuum model analysis for two-dimensional graphene shows that in the presence of an external magnetic field, foldlike deformations generate new states within the LLs, which can be characterized by $\gamma = l_B/b$, the ratio between the magnetic length $l_B = \sqrt{\hbar/eB}$ and the deformation width b [26]. This parameter can be used as a guide to define different regimes of valley filter realizations. In the system considered here, since the central conductor is finite, with the same width as the zigzag terminal leads, we will show the relevance of a third parameter related to the deformation, the ratio between the central conductor and the deformation widths L_Z/b, called the strain spread in the system.

We adopt the mode-matching method [47–49] that allows a direct analysis of the deformation effects in each valley. The transmission matrix elements for one electron in mode m coming from the pth terminal scattered to mode n in the lth terminal is written as [48]

$$t_{l,p}^{k,n,m} = \sqrt{\frac{v_{l,n}}{v_{p,m}^k}} \left[(u_{l,n})^\dagger G(E) [G^0(E)]^{-1} u_{p,m}^k \right], \quad (5)$$

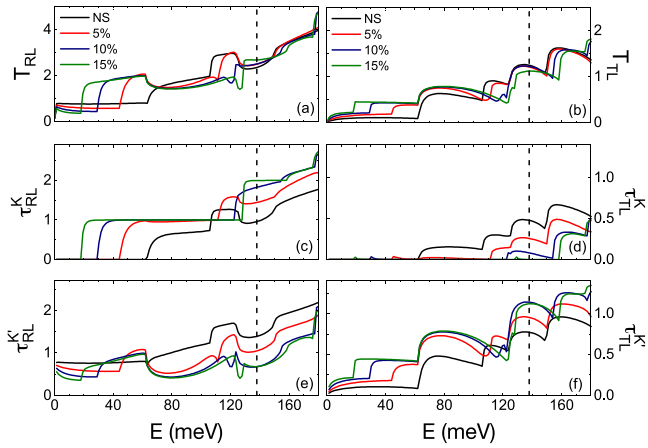

FIG. 2. Total and valley-dependent transmission coefficients between (a), (c), and (e) the left and right terminals and (b), (d), and (f) left and top leads for the unstrained system (NS) and increasing strain intensities with $\alpha = 5\%$, 10%, and 15%. Parameters are $L_Z = 42.5$ nm, $L_A = 29.3$ nm, and $b = 30a_c$.

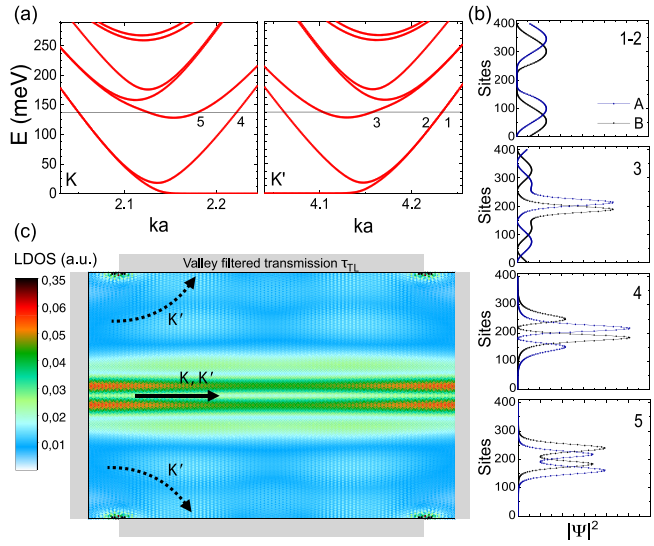

FIG. 3. (a) Band structure of a folded zigzag nanoribbon. (b) Probability density of states at $E = 138$ meV corresponding to the momenta labeled 1, 2, and 3 (K' valley) and 4 and 5 (valley K) in (a). Blue and black symbols indicate the probability densities of the A and B sublattices, respectively. (c) LDOS of the central part of an equivalent four-lead system at the same energy as in (b). Schematic black dashed arrows in (c) indicate valley filtered left to top (and bottom) transmission. The solid black arrow pointing from left to right corresponds to nonpolarized transmission in this direction. Parameters are $L_Z = 42.5$ nm, $L_A = 29.3$ nm, $b = 30a_c$ $A_f = 11.6a_c$, and $\alpha = 15\%$.

where $u_{l,n}$ is the terminal eigenvector in the propagating mode n, $v_{l,n}$ is the Bloch velocity for the nth mode, and k is the valley index ($k = K, K'$). The Green's functions of the full system and the terminals, $G(E)$ and $G^0(E)$, respectively, are obtained with standard iterative techniques [50,51].

The total transmission obtained from k-valley injected electrons is defined as

$$\tau^k_{l,p} = \sum_{m,n} \left| t^{k,n,m}_{l,p} \right|^2, \tag{6}$$

which allows the total transmission calculation [52], $T_{l,p} = \sum_k | \tau^k_{l,p} |^2$.

III. VALLEY TRANSPORT IN THE STRAINED SYSTEM

We analyze first the effect of the extended deformation on the transport properties of the multiterminal system, focusing on the valley-dependent transport responses. The total transmission results, T_{RL} and T_{TL}, are shown in Figs. 2(a) and 2(b), respectively, for fold structures with no strain (NS) and different maximum strain intensities. Due to the system symmetry, the transmissions T_{TL} and T_{BL} are the same, as expected. Valley-dependent transmission components T_{RL} and T_{TL} are depicted in Figs. 2(c) and 2(d) for the K valley and Figs. 2(e) and 2(f) for the K' valley. Note that for the undeformed four-terminal devices (black curves), for energies below approximately 65 meV, only the edges states corresponding to the K' valley contribute to the left to right (left panels) and left to top (right panels) transmissions. This feature is expected for the first plateau in the zigzag nanoribbon leads. Then, the four-terminal system's geometry allows the filtering of K'-valley electrons corresponding to the edges states of the zigzag leads. When the deformation is introduced, the mechanical perturbation induces other plateaus' formation at lower energies [Figs. 2(a) and 2(b)]. The left to top transport is still formed essentially by the K'-valley electrons, which generate a valley polarized current in larger energy ranges depending on the strain intensity. As the deformation increases, the enhancement of the valley filtering process in the left to top transmission [Figs. 2(d) and 2(f)] is followed by an increase of the left to right transmission [Figs. 2(c) and 2(e)]. But the longitudinal transmission T_{RL} is given by a combination of both valley contributions, except for a small energy range, near zero.

To better characterize the deformation effects, taking into account the fact that electrons are injected from the left terminal, we show in Fig. 3(a) the electronic band structure of a zigzag nanoribbon with the same width L_Z as the central part of the four-lead system. Figure 3(b) illustrates the spatial distribution of the probability density of the states that contribute to a particular energy value equal to $E = 138$ meV, marked in Fig. 3(a). Different from the results of the unperturbed system where the states are spread along the whole nanoribbon (not shown), in the deformed system, a high electronic concentration is observed in the deformation region [note in Fig. 3(b) the states labeled 3 at the K' valley and 4 and 5 at the K valley, with positive velocities]. In contrast, the other electronic states, 1 and 2, coming from the K' valley, are localized at the ribbon edges. These states contribute to the valley polarized transmission from the left to top/bottom leads when transverse leads are connected to the central system in the four-lead configuration. The confinement introduced by the extended deformation is easier to understand as a consequence of the pseudomagnetic field. The current injected along the deformed system is expected to be divided into two main contributions: One is along the center of the deformation with a high density of states, formed by states from both

valleys, and the other contribution, at the fold tails, is formed by the states from the K' valley. In the four-lead configuration, these states leak to the top and bottom contacts, making the filter process feasible at higher energies. These features are summarized in the LDOS for the four-lead configuration, shown in Fig. 3(c), where the schematic arrows highlight the discussed valley-selective transport in the system.

As discussed, the addition of new contacts (top and bottom), combined with the deformation effect, creates a favorable scenario for getting valley polarized currents. Previous studies, however, demonstrated that the electronic transport is affected by edge roughness in nanoribbons [26,53]. To eliminate possible effects of edge disorder, we propose applying a magnetic field in the system to achieve suitable conditions for valley filter transport, considering much smaller strain intensities. As we show next, the states propagating in the deformation's central region give rise to the polarized current, with the valley filter happening in the left-right current direction.

IV. SWITCHING THE VALLEY FILTER DIRECTION WITH A MAGNETIC FIELD

To guarantee the formation of the LLs, magnetic field values of the order of 25 T were considered first. However, as we will show, this analysis works equally well for experimentally feasible magnetic field values.

Results for the electronic band structure and the probability density of the states contributing at energy $E/E_1 = 1.1$ are presented in Fig. 4 for the same zigzag nanoribbon discussed in Fig. 3, now under the effect of magnetic field $B = 25$ T, for a smaller strain intensity. The energies are given in terms of the first Landau state, $E_1 = 3\lambda_0 a_c\sqrt{2}/2l_B$. For comparison, Fig. 4(a) shows the system band structure without mechanical deformation, indicated by the black curve. The inhomogeneous pseudomagnetic field forms new dispersive states, characterized by states with maximum and minimum energies for each level.

The probability densities for the momentum states labeled 1, 2, and 3 are depicted in Figs. 4(b) for both sublattices (black and blue symbols). States 1 (K' valley) and 3 (K valley) are localized closer to the top edge. These states would be driven to a top contact if connected. Reversing the magnetic field direction should move the states to the bottom contact. Otherwise, state 2 comes from the K' valley, localized in the ribbon's center. This state is responsible for the K'-filter phenomenon observable in the left-right transmission T_{RL} for this particular energy. This filter takes place not only at that energy but in an energy range labeled ΔE_F [light purple shaded strip in Fig. 4(a)]. The filter range is revealed in the transmission results shown in Fig. 4(c) for the four-contact device (light gray shaded strip) with only the K'-valley contribution, in contrast to the results for the two-contact setup (nanoribbon), where the two valleys contribute to the transmission.

The LDOS maps in the four-lead system help to identify the spatial electronic distribution, as shown Figs. 4(d) and 4(e) at energies $E/E_1 = 0.90$ and 1.07, respectively. The LDOS at energy $E/E_1 = 0.90$ shows some electronic concentration in

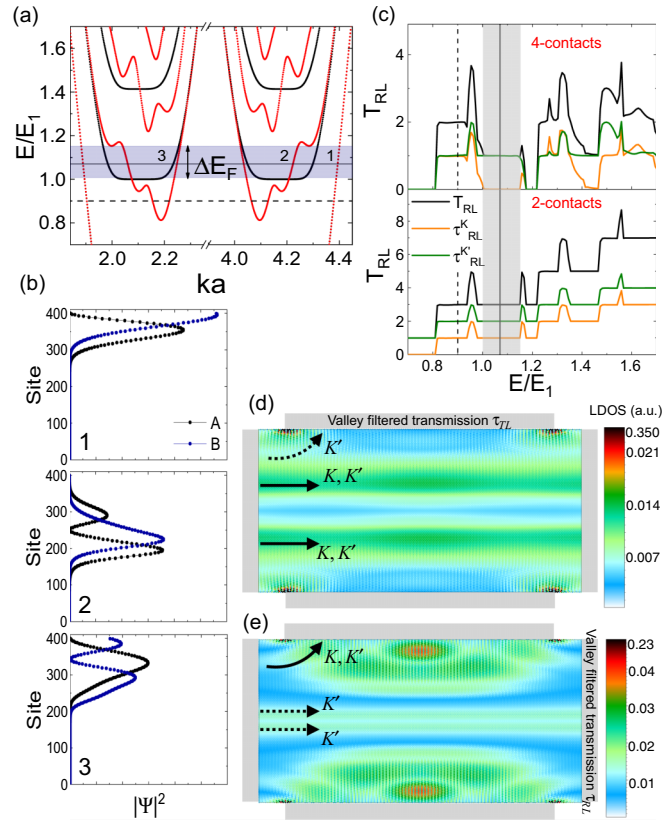

FIG. 4. (a) Band structure of a strained (red) and unstrained (black) zigzag nanoribbon with $B = 25$ T. (b) Probability density at energy $E/E_1 = 1.07$ for the momentum states labeled 1 and 2 (K' valley) and 3 (K valley). Blue and black curves indicate the probability densities of the A and B sublattices, respectively. (c) Comparison of transmission coefficients from the left to right terminals T_{RL} for deformed systems with four and two contacts and $B = 25$ T. Green and orange curves indicate the transmission of the K' and K valleys, respectively. LDOS for the four-lead system at energy (d) $E/E_1 = 0.90$ and (e) $E/E_1 = 1.07$. Dashed (solid) arrows indicate valley filtered (nonfiltered) transmission. Parameters are $L_Z = 42.5$ nm, $L_A = 29.3$ nm, $b = 40a_c$, and $A_f = 8.9a_c$.

the central part of the system, also exhibiting higher electronic distribution closer to the interface with the top and bottom leads due to polarized edge states that flow to top leads. In contrast, at $E/E_1 = 1.07$, a higher electronic concentration is noticeable at the top and bottom contact entrances, highlighted by the orange-colored LDOS. In the central part of the system, some localization is still present. One should take into account that in contrast to the information obtained from the probability density of the individual k states, discussed in Fig. 4(b), the LDOS counts the full contribution at a particular energy, which includes the probability density of states with both velocity directions. The selected velocity direction defines the electronic carrier flux. In the present case, choosing the electron departing from the left terminal, the magnetic field pushes the carrier to the top lead unless it gets trapped in the deformation due to the pseudomagnetic field confinement. An analysis of the valley-dependent transmission indicates a mixed contribution of the K and K' valleys in the top

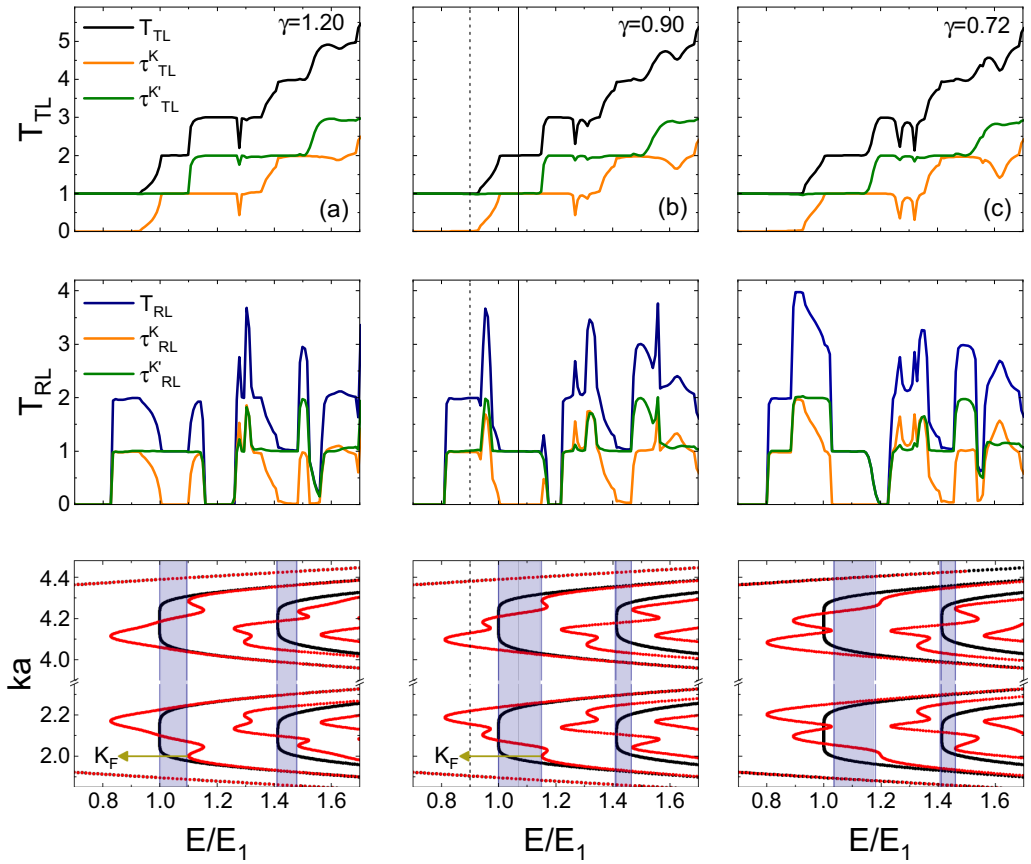

FIG. 5. Top: Transmission coefficients from the left to top terminals T_{LT} (first row) and left to right T_{LR} (second row) for a fold zigzag nanoribbon with $B = 25$ T and γ equal to (a) 1.20, (b) 0.90, and (c) 0.72. The orange and green curves indicate transmission from the K and K' valleys, respectively. Parameters are $L_Z = 42.5$ nm, $L_A = 29.3$ nm, $\alpha = 5\%$, and (a) $b = 30a_c$, (b) $b = 40a_c$, and (c) $b = 50a_c$. Bottom: Corresponding band structures for the strained (red curves) and unstrained (black curves) zigzag ribbons.

contact. Simultaneously, in the left-right direction, polarized carriers are present, as will be discussed next. To investigate the transport through the individual leads and the filter process's dependence on the magnetic field intensity, we calculate the transmission components, considering an electron flowing from the left terminal.

We discuss the competition between the localization mechanisms introduced by strain and magnetic field in terms of the parameter $\gamma = l_B/b$.

The transmission results for the four-lead system with different γ values are shown in Fig. 5. Different from the case of zero field, the transmission from the left to bottom leads (not shown) goes to zero, $T_{BL} = 0$, due to the Lorentz force. On the other hand, the transmission from the left to top T_{TL} is formed by a combination of carriers from both the K and K' valleys, as can be seen in the first row in Figs. 5(a)–5(c) (orange and green curves). The left to right transmission results, presented in the second row, show that only the K' valley contributes in some energy windows. This feature confirms that it is possible to switch the valley filter to the left-right direction when the magnetic field is turned on. It is interesting to note that without the deformation, left to right transmission should be null in the quantum Hall regime since the current goes directly to the top lead due to Lorentz force. However, with deformation, extra current channels will be detected in the experiments. In fact, single-channel left to right transmission ($2e^2/h$, two per spin) is expected to appear at energies just above the first Landau level, being a fingerprint of the polarized currents, assuming the spin degeneracy is not broken in the system.

We show next further analysis to identify the filtering energy window dependence on the system's parameters. As mentioned, the filter region is closely related to the features of the zigzag nanoribbon terminals' electronic structure. We observe in the case of $\gamma = 1.20$ and $\gamma = 0.90$ that ΔE_F is bounded between the first LL energy (thick black line) and the minimum energy value marked by k_F in the bottom panels of Figs. 5(a) and 5(b), which touch the shaded light purple strips. The momentum k_F corresponds to the minimum energy limiting the valley filter region. For smaller γ parameters, new states of maximum and minimum energies are formed in the band structure, overcoming the first LL. This feature is seen in the case of $\gamma = 0.72$, where ΔE_F is now between a maximum and the minimum of the energy [bottom panel of Fig. 5(c)].

V. VALLEY FILTER WINDOWS: SYSTEM'S DEPENDENCE ON CONFINEMENT PARAMETERS

We propose an energy filter route to predict the valley filter window in terms of controllable parameters given by the magnetic field, strain intensity, and ribbon widths. We

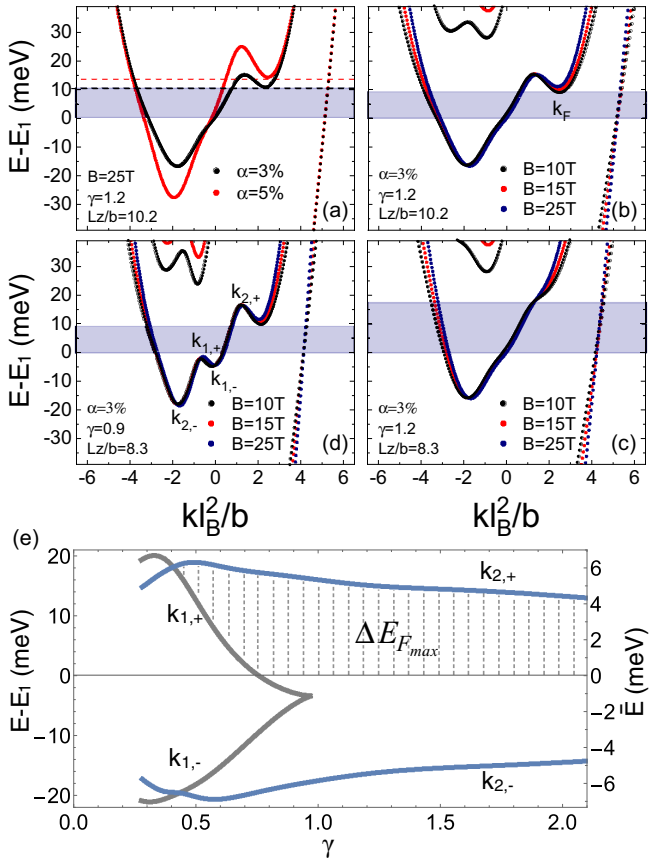

FIG. 6. Band structure of fold zigzag nanoribbons with energy given with respect to the first LL of the unperturbed system. (a) $B = 25$ T, $\gamma = 1.2$, $L_Z/b = 10.2$, and strain intensities $\alpha = 3\%$ and 5%, depicted by black and red curves, respectively. (b) and (c) Comparison between different values of $B = 10$, 15, and 25 T for $L_Z/b = 10.2$ and 8.3, respectively, with $\alpha = 3\%$ and $\gamma = 1.2$. (d) Comparison between the same magnetic field values, with $\gamma = 0.9$, $L_Z/b = 8.3$, and $\alpha = 3\%$. Extreme energy variations are labeled by the momentum values k_F, $k_{1,\pm}$, and $k_{2,\pm}$. (e) Energy filter window as a function of γ, defined by the extreme energy corrections given by the momentum values labeled as in (d).

alternatively propose a description of the strain effect by the amount of deformation spread in the ribbon width, given by L_Z/b, a large ratio pointing to a weak spread of the system's deformation. The energy bands of fold zigzag nanoribbons for different combinations of γ and L_Z/b and magnetic field intensities are shown in Fig. 6. The carrier's energies are defined with respect to the first LL of the unstrained system $(E - E_1)$. Also, to better visualize the magnetic field effect on the electronic structure of unstrained nanoribbons, an effective dimensionless momentum is usually adopted [54], kl_B^2/L_Z. Here we propose a similar renormalized momentum, given in terms of the deformation extension kl_B^2/b.

To highlight the strain effect through the new parameter L_Z/b, we present in Figs. 6(a)–6(d) band structure results, taking fixed values of this ratio in each panel. In Fig. 6(a) we compare the predictions obtained by longitudinal transmission results for the valley filter window ΔE_F at a fixed magnetic field value of $B = 25$ T for strains $\alpha = 3\%$ and 5%, marked by the light purple shaded strip and red dashed line, respectively. The results reveal an increased filtering energy window for higher α intensity. Within the proposed momentum scale, changes in the magnetic field intensities ($B = 10$, 15, and 25 T) slightly modify the energy filter range, as can be seen in Figs. 6(b) to 6(d). The light purple shaded strips in Figs. 6(b)–6(d) correspond to the valley filtering windows for the left to right transmission coefficients obtained with $B = 10$ T. The momentum k_F [Fig. 6(b)] related to the minimum energy value limits the valley filter region.

Comparing the band structures depicted in Figs. 6(b) and 6(c) and the corresponding filter energies for two different values of L_Z/b, we conclude that a reduction in L_Z/b from 10.2 to 8.3 affects the edges states, pushing the states positioned at the deformation tails to the top contact. The valley filter window efficiency in the longitudinal direction is then enhanced in a larger window. Otherwise, a direct comparison between Figs. 6(c) and 6(d) for a fixed L_Z/b ratio equal to 8.3 indicates that the filter region is larger for $\gamma = 1.2$ than for $\gamma = 0.9$. Smaller γ implies electrons are more confined in the deformation region, decreasing the filter window efficiency.

We obtain the maximum valley filter energy window by mapping the extreme energy values (maxima and minima) in the zigzag carrier's band structure. The states with extreme energy values are labeled $k_{1,\pm}$ and $k_{2,\pm}$, as shown in Fig. 6(d). The evolution of the extreme energies as a function of γ is presented in Fig. 6(e) for $\alpha = 3\%$. Alternatively, the right axis is scaled as $\bar{E} = (E - E_1)/\alpha$. This energy scale is possible due to the linear dependence of the energy variation on the strain α, as predicted by perturbation theory [26]. A small asymmetry of the energy variation concerning the first LL (horizontal line at zero) is found that is more noticeable for the $k_{1,\pm}$ states. The states $k_{1,\pm}$ rise as energy extrema for $\gamma < 1$, with energy correction lower than the first LL. For values of $\gamma < 0.4$, the energy of the state $k_{1,+}$ is larger than the first LL. A comparison of these results with longitudinal transmission calculations allowed the identification of the maximum valley filter energy window $\Delta E_{F_{\max}}$, highlighted with grid lines Fig. 6(e). We find two different regimes; for $\gamma > 0.75$, the filter window is given by the energy difference between states $k_{2,+}$ and the first LL energy. For $\gamma < 0.75$, energy deviations for states $k_{1,+}$ are larger than zero; then the valley filter window is given by the energy difference between states $k_{1,+}$ and $k_{2,+}$. This energy difference starts to decrease for γ smaller than 0.75 and around $\gamma = 0.4$ is closed, indicating a lower boundary for valley filtering energy processes.

Finally, we show in Fig. 7 the dependence of the valley filter energy window on the strain ratio L_Z/b for different γ values, $B = 10$ T, and $\alpha = 3.0\%$. The individual curves correspond to a fixed γ ratio. Notice that values of γ around 0.8 have larger filter energy windows. Moreover, there will be a minimum value for γ at which the valley filter goes to zero, as discussed previously. Meanwhile, the spread of strain in the system L_Z/b was also shown to be extremely relevant for enhancing the valley filtering energy window. The evolution of the curves maps an energy-topography diagram that defines ideal parameter ranges $[\gamma \times (L_Z/b)]$ for the occurrence of valley filtering. For example, to achieve valley filtering in the left to the right transmission for $\gamma = 0.83$, the L_Z/b range

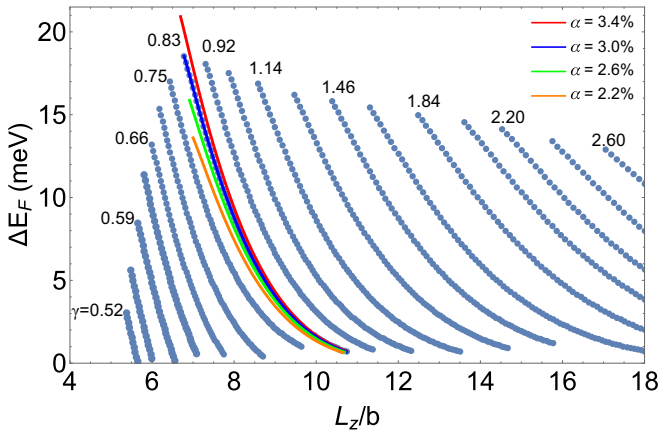

FIG. 7. Energy dependence of the K'-valley filtered left to right transmission on the four-lead system confinement parameters, γ, and L_Z/b for a fixed magnetic field $B = 10$ T and strain intensity $\alpha = 3.0\%$ (blue curves). Valley filtering energy window dependence on α values (red, green, and orange lines) for $\gamma = 0.83$.

should be between 7.5 and 10.5. Also shown in Fig. 7 is the energy dependence of the K'-valley filtered transmission on the α strain parameter for $\gamma = 0.83$, with α varying from 2.2% to 3.4%. Small changes in the curve are observed, mainly in the intensity, with the filter energy window varying from 14 to 21 meV, but with almost the same L_Z/b window, which is a bit larger for larger α. This analysis is valid for $\alpha < 3.5\%$. The valley filter energy window starts to decrease for higher strain values since other states from the second LL start to contribute to the transmission at the same energy window.

VI. CONCLUSION

Multiterminal graphene systems were addressed as appropriate setups for valley filtering and switches of valley polarized current directions. Using the mode-matching model based on the Green's function formalism, we showed that strain enhances the valley filtering processes in graphene multiterminal configurations. For extended folds in the longitudinal directions, currents flowing from left to top/bottom leads are valley polarized, with larger energy windows for higher strain intensity. An external magnetic field improves the deformation effects on the valley filter processes, avoiding undesirable disorder outcomes and generating valley filter energy windows for lower strain intensities. Adding the magnetic field also switches the valley filter direction in some energy windows, with valley filtered transmission from the left to the right contacts. We showed a diagram analyzing the interplay between the confinement parameters that maps the valley filter energy window, including the dependence on the strain intensity α, the strain spread L_Z/b, and the ratio between the magnetic length and the deformation extension γ. We hope this analysis motivates the development of other works with experimental measurements and applications of valley polarized electronic currents.

ACKNOWLEDGMENTS

This work was financially supported by the Brazilian Agencies CAPES, CNPq, and FAPERJ under Grant No. E-26/202.567/2019 and the INCT de Nanomateriais de Carbono. V.T. is thankful for Grant No. E-26/202.322/2018 from FAPERJ. We are grateful to N. Sandler for helpful discussions.

[1] J. Nakabayashi, D. Yamamoto, and S. Kurihara, Phys. Rev. Lett. **102**, 066803 (2009).
[2] J. R. Schaibley, H. Yu, G. Clark, P. Rivera, J. S. Ross, K. L. Seyler, W. Yao, and X. Xu, Nat. Rev. Mater. **1**, 1 (2016).
[3] M. Settnes, J. H. Garcia, and S. Roche, 2D Mater. **4**, 031006 (2017).
[4] A. Rycerz, J. Tworzydło, and C. W. J. Beenakker, Nat. Phys. **3**, 172 (2007).
[5] D. Gunlycke and C. T. White, Phys. Rev. Lett. **106**, 136806 (2011).
[6] R. V. Gorbachev, J. C. W. Song, G. L. Yu, A. V. Kretinin, F. Withers, Y. Cao, A. Mishchenko, I. V. Grigorieva, K. S. Novoselov, L. S. Levitov, and A. K. Geim, Science **346**, 448 (2014).
[7] A. R. S. Lins and J. R. F. Lima, Carbon **160**, 353 (2020).
[8] N. Myoung, H. Choi, and H. C. Park, Carbon **157**, 578 (2020).
[9] Y. S. Ang, S. A. Yang, C. Zhang, Z. S. Ma, and L. K. Ang, Phys. Rev. B **96**, 245410 (2017).
[10] J. Li, R. X. Zhang, Z. Yin, J. Zhang, K. Watanabe, T. Taniguchi, C. Liu, and J. Zhu, Science **362**, 1149 (2018).
[11] R. Carrillo-Bastos, C. León, D. Faria, A. Latgé, E. Y. Andrei, and N. Sandler, Phys. Rev. B **94**, 125422 (2016).
[12] M. Settnes, S. R. Power, M. Brandbyge, and A.-P. Jauho, Phys. Rev. Lett. **117**, 276801 (2016).
[13] S. P. Milovanović and F. M. Peeters, Appl. Phys. Lett. **109**, 203108 (2016).
[14] E. Andrade, R. Carrillo-Bastos, and G. G. Naumis, Phys. Rev. B **99**, 035411 (2019).
[15] G. W. Jones, D. A. Bahamon, A. H. Castro Neto, and V. M. Pereira, Nano Lett. **17**, 5304 (2017).
[16] V. Torres, P. Silva, E. A. T. de Souza, L. A. Silva, and D. A. Bahamon, Phys. Rev. B **100**, 205411 (2019).
[17] T. Stegmann and N. Szpak, 2D Mater. **6**, 015024 (2018).
[18] R. Carrillo-Bastos, M. Ochoa, S. A. Zavala, and F. Mireles, Phys. Rev. B **98**, 165436 (2018).
[19] A. Georgi, P. Nemes-Incze, R. Carrillo-Bastos, D. Faria, S. Viola Kusminskiy, D. Zhai, M. Schneider, D. Subramaniam, T. Mashoff, N. M. Freitag *et al.*, Nano Lett. **17**, 2240 (2017).
[20] D. Zhai and N. Sandler, Phys. Rev. B **98**, 165437 (2018).
[21] N. M. Freitag, T. Reisch, L. A. Chizhova, P. Nemes-Incze, C. Holl, C. R. Woods, Y. C. Gorbachev, K. S. Geim, Novoselov, J. Burgdörfer, F. Libish, and M. Morgenstern, Nat. Nanotechnol. **13**, 392 (2018).
[22] S.-Y. Li, Y. Su, Y.-N. Ren, and L. He, Phys. Rev. Lett. **124**, 106802 (2020).
[23] S.-Y. Li, K.-K. Bai, L.-J. Yin, J.-B. Qiao, W.-X. Wang, and L. He, Phys. Rev. B **92**, 245302 (2015).

[24] N. N. Klimov, S. Jung, S. Zhu, T. Li, C. A. Wright, S. D. Solares, D. B. Newell, N. B. Zhitenev, and J. A. Stroscio, Science **336**, 1557 (2012).
[25] V. Torres, D. Faria, and A. Latgé, Phys. Rev. B **97**, 165429 (2018).
[26] D. Faria, C. León, L. R. F. Lima, A. Latgé, and N. Sandler, Phys. Rev. B **101**, 081410(R) (2020).
[27] T. Fujita, M. B. A. Jalil, and S. G. Tan, Appl. Phys. Lett. **97**, 043508 (2010).
[28] T. Low and F. Guinea, Nano Lett. **10**, 3551 (2010).
[29] D. Rainis, F. Taddei, M. Polini, G. León, F. Guinea, and V. I. Fal'ko, Phys. Rev. B **83**, 165403 (2011).
[30] K.-J. Kim, Y. M. Blanter, and K.-H. Ahn, Phys. Rev. B **84**, 081401(R) (2011).
[31] Z. Qi, D. Bahamon, V. M. Pereira, H. S. Park, D. K. Campbell, and A. H. C. Neto, Nano Lett. **13**, 2692 (2013).
[32] B. Roy, Z.-X. Hu, and K. Yang, Phys. Rev. B **87**, 121408(R) (2013).
[33] T. Farajollahpour and A. Phirouznia, Sci. Rep. **7**, 1 (2017).
[34] A. H. Castro Neto, F. Guinea, N. M. R. Peres, K. S. Novoselov, and A. K. Geim, Rev. Mod. Phys. **81**, 109 (2009).
[35] S. R. Power, M. R. Thomsen, A.-P. Jauho, and T. G. Pedersen, Phys. Rev. B **96**, 075425 (2017).
[36] M. Yamamoto, O. Pierre-Louis, J. Huang, M. S. Fuhrer, T. L. Einstein, and W. G. Cullen, Phys. Rev. X **2**, 041018 (2012).
[37] L. Tapasztó, T. Dumitrică, S. J. Kim, P. Nemes-Incze, C. Hwang, and L. P. Biró, Nat. Phys. **8**, 739 (2012).
[38] V. Calado, G. Schneider, A. Theulings, C. Dekker, and L. Vandersypen, Appl. Phys. Lett. **101**, 103116 (2012).
[39] H. Lim, J. Jung, R. S. Ruoff, and Y. Kim, Nat. Commun. **6**, 8601 (2015).
[40] Y. Jiang, J. Mao, J. Duan, X. Lai, K. Watanabe, T. Taniguchi, and E. Y. Andrei, Nano Lett. **17**, 2839 (2017).
[41] C. Ma, X. Sun, H. Du, J. Wang, M. Tian, A. Zhao, Y. Yamauchi, and B. Wang, Nano Lett. **18**, 6710 (2018).
[42] M. G. P. Carbone, A. C. Manikas, I. Souli, C. Pavlou, and C. Galiotis, Nat. Commun. **10**, 1 (2019).
[43] V. Torres, C. León, D. Faria, and A. Latgé, Phys. Rev. B **95**, 045425 (2017).
[44] M. A. Vozmediano, M. Katsnelson, and F. Guinea, Phys. Rep. **496**, 109 (2010).
[45] M. I. Katsnelson and K. S. Novoselov, Solid State Commun. **143**, 3 (2007).
[46] F. de Juan, J. L. Mañes, and M. A. H. Vozmediano, Phys. Rev. B **87**, 165131 (2013).
[47] T. Ando, Phys. Rev. B **44**, 8017 (1991).
[48] P. A. Khomyakov, G. Brocks, V. Karpan, M. Zwierzycki, and P. J. Kelly, Phys. Rev. B **72**, 035450 (2005).
[49] H. H. B. Sørensen, P. C. Hansen, D. E. Petersen, S. Skelboe, and K. Stokbro, Phys. Rev. B **79**, 205322 (2009).
[50] C. H. Lewenkopf and E. R. Mucciolo, J. Comput. Electron. **12**, 203 (2013).
[51] G. Thorgilsson, G. Viktorsson, and S. Erlingsson, J. Comput. Phys. **261**, 256 (2014).
[52] S. Datta, *Electronic Transport in Mesoscopic Systems* (Cambridge University Press, Cambridge, 1997).
[53] E. R. Mucciolo, A. H. Castro Neto, and C. H. Lewenkopf, Phys. Rev. B **79**, 075407 (2009).
[54] P. Delplace and G. Montambaux, Phys. Rev. B **82**, 205412 (2010).